Vol. 14, 2025, 217-231

DOI: 10.17512/bozpe.2025.14.22

Construction of optimized energy potential

Budownictwo o zoptymalizowanym potencjale energetycznym

ISSN 2299-8535 e-ISSN 2544-963X

Identification of brittle damage in a UHPC beam using ultrasonic transmission tomography

Karolina Tatara[1*] (*orcid id: 0000-0002-4401-1858*)

Piotr Adam Bońkowski[1] (*orcid id: 0000-0001-9931-9115*)

[1] Opole University of Technology, Poland

Abstract: This paper presents the results of ultrasonic testing conducted on a steel fiber-reinforced UHPC (Ultra-High Performance Concrete) beam with dimensions of 0.2 m × 0.24 m × 6.0 m. The beam was subjected to 13 loading stages, with an asymmetrical load application. For the first 11 loading stages, longitudinal ultrasonic wave propagation at a frequency of 150 kHz was measured prior to each loading step using an ultrasonic concrete tester. The recorded wave travel times were then processed in MATLAB using a least squares method with Tikhonov regularisation to reconstruct the damaged zones within the beam. The results enabled the identification of localised cracks and the progressive development of damage in the UHPC beam.

Keywords: concrete, UHPC, ultrasonic transmission tomography

Please, quote this article as follows:

Tatara, K. & Bońkowski, P.A. (2025) Identification of brittle damage in a UHPC beam using ultrasonic transmission tomography. *Construction of Optimized Energy Potential* (*CoOEP*), 14, 217-231. DOI: 10.17512/bozpe.2025.14.22

Introduction

Diagnostics plays a key role in many branches of engineering, including civil engineering. Diagnostic techniques are commonly classified as destructive, semi-destructive and non-destructive. For obvious reasons, non-destructive methods attract the greatest interest, as they are less labour-intensive and can be applied for continuous monitoring (Smedt et al., 2018; Uhl, 2010). Moreover, they contribute to waste reduction and make it possible to assess the suitability of existing structural concrete elements for reuse (Karatosun et al., 2025). These practices align with the

[*] Corresponding author: k.tatara@po.edu.pl

principles of sustainable development by extending the service life of buildings while simultaneously reducing operation and refurbishment costs. They enable the evaluation of material properties (e.g. stiffness, strength), the detection of discontinuities and the measurement of layer thicknesses without disturbing the integrity of the element. However, both the testing itself and the interpretation of the results require substantial experience and advanced signal processing. The field of *Non-Destructive Testing* (NDT) is developing dynamically, driven by industrial needs for reliability, shortened production cycles and optimised procedures.

Concrete is one of the most widely used materials in construction and, as such, is the focus of attention from the mix design stage through to its service life. From a durability standpoint, a critical drawback of concrete is its brittle behaviour: the initiation and propagation of cracks and fissures increase permeability, reduce strength, and accelerate corrosion processes. This underlines the need for early diagnostics, which enables the implementation of preventive measures. Additionally, a more accurate assessment of ultimate and serviceability limit states, as well as a more reliable interpretation of laboratory test results are needed.

Non-destructive methods are particularly desirable, as they are less labour-intensive, can be used for continuous monitoring, and do not disturb structural integrity, while still providing information on material properties, the presence of discontinuities, and layer thicknesses. Importantly, NDT techniques are relevant not only during the service life of structures, but also at the stages of material production, prefabrication, and the construction of structures of major social importance.

Among the most widely recognised non-invasive methods for identifying defects in concrete are acoustic methods (Drobiec et al., 2010; Lewińska-Romicka, 2001), which include two principal techniques: ultrasonic testing and the impact-echo method.

The ultrasonic method belongs to the group of volumetric testing techniques. It is primarily used to assess selected physical and mechanical properties, as well as to detect internal, surface, and subsurface discontinuities in the material (Drobiec et al., 2010). It consists of introducing acoustic waves (mechanical vibrations) with frequencies higher than the upper limit of human hearing (i.e., > 20 kHz) into the tested element, recording them, and analysing changes in their amplitude and/or propagation time (velocity). The parameters of ultrasonic waves depend on the macroscopic and microscopic properties of the material under investigation, such as density, moisture content, molecular structure, and elastic properties.

The impact-echo method differs from ultrasonic testing in both the measurement equipment used and the processing and interpretation of the recorded signals. It is based on the propagation of stress waves in solids generated by striking the surface of the tested element with a special instrumented impact hammer, hence the name of the method. The response is evaluated using the *Impact-Echo* (IE) technique, which consists of analysing the frequency spectrum of the reflected waves.

In practice, both techniques perform very well in detecting more advanced damage, where the wave either bypasses the damaged zone or is reflected by it. However, for the identification of early-stage, weakly developed damage, imaging of the internal structure by means of ultrasonic tomography is particularly useful.

1. Ultrasonic tomography (UT)

Ultrasonic Tomography (UT) is used to obtain information on the condition of the internal structure of the material under investigation (Śliwiński, 2001). It is based on the mathematical reconstruction of selected projections of acoustic parameters characterising the material structure, most commonly using measurements of the mean travel time of an ultrasonic pulse along the transmitter-receiver path (Polakowski & Sikora, 2016). Four basic types of ultrasonic tomography are presented in Figure 1.

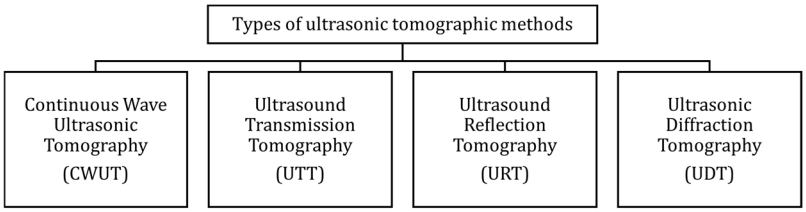

Fig. 1. Types of ultrasonic tomographic methods (*own study based on* Opieliński et al., 2002)

In concrete elements at low levels of mechanical loading, the cracks do not yet form clearly localised discontinuities capable of effectively reflecting the ultrasonic signal. The method is particularly effective under conditions where: a) the acoustic impedances of both subdomains are identical (Fig. 2a), or the acoustic impedance of subdomain 2 is slightly lower (Fig. 2b).

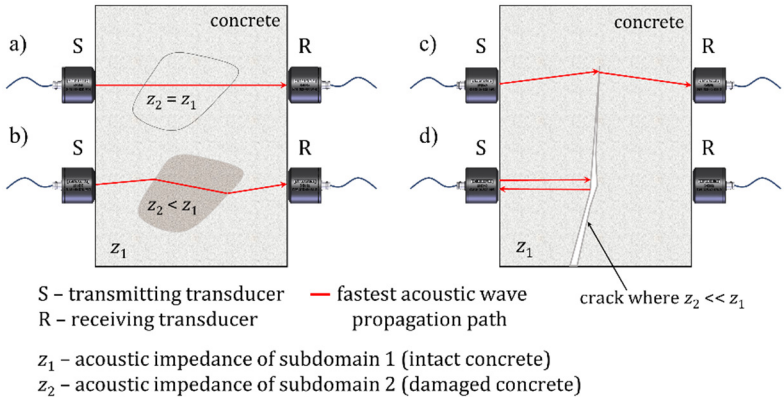

Fig. 2. Cases of wave transmission through a concrete element with an elastically degraded zone (a, b) and with a crack: a) the acoustic impedances of both subdomains are identical ($z_2 = z_1$), b) the acoustic impedance of subdomain 2 is slightly lower ($z_2 < z_1$), c) and d) the acoustic impedance of subdomain 2 is significantly lower ($z_2 \ll z_1$) (*own research*)

When the impedance values differ significantly (e.g., for a void or an air-filled discontinuity, $z_2 \ll z_1$), the transmission of the ultrasonic wave is strongly disturbed. In such cases, the incident wavefront is forced to bypass the defect by diffracting around its edges (Fig. 2c) or is almost completely reflected at the interface (Fig. 2d).

In general terms, this method consists of extracting information contained in ultrasonic pulses recorded after transmission through the tested object (Kak & Slaney, 1999; Opieliński & Gudra, 2002), for example, by identifying local reductions in ultrasonic wave velocity within cracked zones of concrete elements.

1.1. Ultrasonic transmission tomography (UTT)

Ultrasonic Transmission Tomography (UTT) utilises the information contained in the ultrasonic signal after it has propagated through the medium under investigation. Measurements are performed along paths (so-called rays) between transmitting and receiving points, recording either the signal travel time or its attenuation coefficient at a given frequency, or, alternatively, the frequency derivative of the attenuation coefficient (Polakowski & Sikora, 2016). On this basis, after appropriate mathematical reconstruction, a tomographic image of the internal structure of the medium is obtained and indirectly represented by maps visualising the spatial distributions of ultrasonic wave velocity or attenuation coefficient. When measuring the travel time of an ultrasonic pulse, it should be noted that excitation of mechanical waves in the tested element may generate several wave types. In such cases, the analysis focuses on those wave modes that propagate fastest (e.g., bulk longitudinal waves in massive elements) or that dominate the recorded response (e.g., Lamb waves in plates (Perkowski et al., 2018)). Their average velocity can be estimated from the measured propagation time between transmitter and receiver, under the simplifying assumption that the fastest paths of sound propagation are straight.

To determine the spatial distribution of this quantity, an appropriate system of equations must be formulated (see, for example, Kak & Slaney, 1999). The reconstructed image is assumed to consists of a finite number of pixels. A computational grid composed of N rectangular cells of dimensions $\delta_1 \times \delta_2$ (Fig. 3), is superimposed on the examined element, with each cell corresponding to a single pixel.

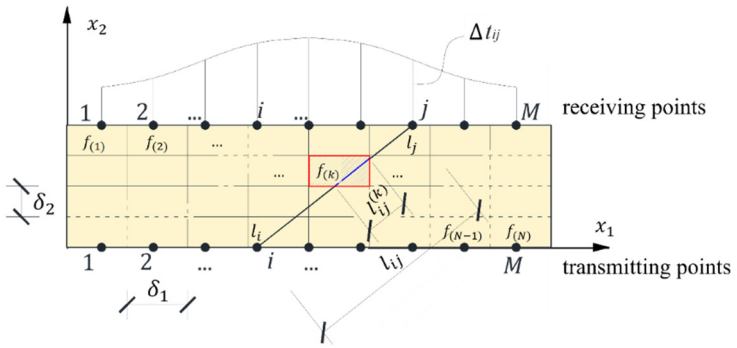

Fig. 3. Scheme of a cell system, transmitting/receiving points, and rays in a plane area examined tomographically (*own research*)

The unknown function $f(x, y)$ in the investigated domain is then approximated in a piecewise constant form by assuming that, within each cell, it takes a constant value $f_{(k)}(k = 1,2, \dots, N)$.

Subsequently, if reconstruction of the material structure is based on measurements of the ultrasonic time-of-flight between transmitting points $i = 1,2, \dots, M$ and receiving points $j = 1,2, \dots, M$, the measured travel time is related to the pulse propagation velocity and to the geometry of the path (ray) along which it propagates by the following expression:

$$\Delta t_{ij} = \int_{l_i}^{l_j} \frac{1}{c(l)} dl, \tag{1}$$

where:
c – longitudinal wave velocity as a function of position along the ray [m/s];
l – coordinate along the ray connecting points i and j whose positions are denoted by l_i and l_j, respectively [m];
Δt_{ij} – travel time of the pulse from point i to point j [s].

Consequently, in the present formulation the unknown function f is defined as the reciprocal of the wave velocity c. Moreover, recognising that only averaged values of f within the individual cells are to be determined, we can write:

$$\Delta t_{ij} = \sum_{k=1}^{N} l_{ij}^{(k)} f_{(k)}, \tag{2}$$

where $l_{ij}^{(k)}$ – length of the segment of the ray $l_{ij} = |l_i l_j|$ contained within the k-th cell (if the ray does not intersect the cell k, then $l_{ij}^{(k)} = 0$) [m].

The above expression defines a system of equations with respect to the unknowns $f_{(k)}$, which is used to determine the distribution of ultrasonic wave propagation velocity in tomography. Upon solving this system, one obtains:

$$c_{(k)} = \frac{1}{f_{(k)}}, \tag{3}$$

where $c_{(k)}$ – the average velocity (in the sense of the present method) of the identified wave mode in the k-th cell [m/s].

One limitation of the adopted formulation is that, for ultrasonic waves that may diffract when passing through regions with different acoustic impedances, the actual ray geometry is not known. Therefore, it is assumed, as a simplification, that the rays $l_i l_j$ are straight-line segments connecting points i and j. This assumption is one of the primary sources of error in the method, particularly when the investigated element contains subdomains whose acoustic impedance differs significantly from that of the surrounding material.

The number of rays $l_i l_j$ employed must be at least equal to the assumed number M. For notational convenience, system (2) is written in the following matrix form:

$$\mathbf{Ax} = \mathbf{b}, \tag{4}$$

where:

$\mathbf{A} = \left[A_{ij}\right]_{P\mathrm{x}N}$ – coefficient matrix [m];

$\mathbf{x} = \left[f_{(1)}, f_{(2)}, \ldots, f_{(N)}\right]^{T}_{1\mathrm{x}N}$ – vector of unknowns, whose components are equal to the reciprocals of the ultrasonic wave propagation velocity in the individual cells [s/m];

$\mathbf{b} = [\Delta t_{11}, \Delta t_{12}, \ldots]^{T}_{1\mathrm{x}P}$ – vector of measured wave travel times along the individual rays [s];

P – number of rays $l_i l_j$.

In tomographic inverse problems, the linear system (4) is typically severely ill-conditioned, because the system matrix **A** is non-banded and exhibits a large condition number, i.e. small perturbations in the data vector **b** may produce large relative errors in the solution vector **x**. Consequently, the tomographic reconstruction problem should be solved using iterative algorithms, often in combination with regularisation techniques.

1.2. Method used for image reconstruction

A fundamental tomographic image reconstruction method is the iterative projection algorithm introduced by the Polish mathematician Stefan Kaczmarz (1937). In 1970 it was rediscovered and popularised in medical imaging by Gordon and co-workers under the name *Algebraic Reconstruction Technique* (ART) (Gordon et al., 1970). This method was employed in the first X-ray computed tomography (CT) scanner developed by Hounsfield (Hounsfield, 1973).

On the basis of Kaczmarz's algorithm, numerous variants have been developed. In the classical literature, three main families of algebraic methods are distinguished: ART, the *Simultaneous Iterative Reconstruction Technique* (SIRT) and the *Simultaneous Algebraic Reconstruction Technique* (SART), the latter combining advantageous features of both ART and SIRT (Hansen & Saxild-Hansen, 2012; Kak & Slaney, 1999).

Moreover, one of the methods used to solve the linear systems arising in tomography is the least-squares method with Tikhonov regularisation (Phillips, 1962). In Perkowski et al. (2018), reconstructions of the tested elements obtained using ART and Tikhonov-regularised least squares were presented. It was shown that the use of Tikhonov-regularised least squares yields physically realistic velocity maps, which directly translates into a more reliable assessment of the spatial distribution of material stiffness. For this reason, the present study adopts the least-squares method with Tikhonov regularisation.

The classical *Least-Squares* (LS) method provides an approximate solution to overdetermined systems, i.e. when the number of equations exceeds the number of unknowns. Its most common application is linear regression, which determines the parameters of the straight line that best fits (in the least-squares sense) a given set of points in the plane. In general terms, solving the system $\mathbf{Ax} = \mathbf{b}$ in the LS sense consists in finding the minimum of an objective function defined as the sum of squared differences between the components of the vectors **Ax** and **b**:

$$F(x) = \|\mathbf{Ax} - \mathbf{b}\|^2 = min, \tag{5}$$

which leads to the solution of the form:

$$\mathbf{x} = (\mathbf{A}^{\mathrm{T}}\mathbf{A})^{-1}\mathbf{A}^{T}\mathbf{b}. \tag{6}$$

If the system $\mathbf{Ax} = \mathbf{b}$ is ill-conditioned, the stability of its solution can be improved by introducing regularisation. One of the most widely used approaches is Tikhonov regularisation, in which a so-called regularisation term is added to the objective function (5), and the minimum of the resulting functional is sought for an appropriately chosen regularisation parameter α, namely:

$$F(\boldsymbol{x}_\alpha) = \frac{1}{2}\|\mathbf{Ax}_\alpha - \mathbf{b}\|^2 + \frac{1}{2}\alpha\|\mathbf{R}(\mathbf{x}_\alpha - \mathbf{x}_0)\|^2 = min \tag{7}$$

which leads to the regularised normal equations of the form:

$$\mathbf{x}_\alpha = \left(\mathbf{A}^{\mathrm{T}}\mathbf{A} + \alpha\,\mathbf{R}^{\mathrm{T}}\mathbf{R}\right)^{-1}\left(\mathbf{A}^{\mathrm{T}}\mathbf{b} + \alpha\,\mathbf{R}^{\mathrm{T}}\mathbf{R}\mathbf{x}_0\right), \tag{8}$$

where:

$\mathbf{A}, \mathbf{b}$ – coefficient matrix and measurement data vector;

α – regularisation parameter [–];

$\mathbf{x}_\alpha = \left[f_{(1)\alpha}, f_{(2)\alpha}, \ldots, f_{(N)\alpha}\right]_{1xN}^{\mathrm{T}}$ – vector of unknowns, whose components are equal to the reciprocals of the ultrasonic wave propagation velocity in the individual cells for a given value of α [s/m];

$\mathbf{x}_0 = \left[c_{ref}^{-1}, c_{ref}^{-1}, \ldots, c_{ref}^{-1}\right]_{1xN}^{\mathrm{T}}$ – vector whose components are equal to the reciprocals of the reference ultrasonic wave propagation velocities c_0 [s/m];

$\mathbf{R} = \left[R_{ij}\right]_{NxN}$ – regularisation matrix [–].

The structure of the regularisation matrix can be specified in various ways (Lampe & Voss, 2010; Polak & Mroczka, 2007; Voss, 2010). In the simplest formulation, the matrix **R** is taken to be the identity matrix. More generally, **R** can be used to impose desired properties on the regularised solution, provided that some a priori information about the solution is available. In the present study, in order to smooth the regularised solutions by reducing the magnitude of second derivatives in the velocity distribution maps constructed from x_α, the matrix **R** was chosen as a discrete second-order differential operator (Tatara, 2019).

The selection of an appropriate value of the regularisation parameter α, in the present study was based on the *L-curve* criterion (Lawson & Hanson, 1995; Miller, 1970). This is a heuristic parameter-choice rule, in which α is determined as a compromise between the residual term and the regularisation term of functional (7). In a log–log plot of the norm of the residual versus the norm of the regularised solution,

the *L-curve* typically consists of two characteristic branches (Fig. 4). The first is a "flat" branch, where the error is dominated by the regularisation term (increasing α), and the second is a "steep" branch, where the error is governed by perturbations associated with the ill-conditioning of the system $\mathbf{Ax} = \mathbf{b}$ (decreasing α). The optimal value of α is usually located in the vicinity of the corner of the *L-curve* (the point of maximum curvature), where the regularisation is already sufficient to stabilise the solution while still retaining most of the information contained in the residual term of functional (7). In some cases, more than one pronounced corner may appear on the *L-curve* (Skubalska-Rafajłowicz, 2011). In such cases, the corresponding solutions must be assessed from an additional perspective, for example by examining their physical plausibility or by analysing the data misfit, i.e. the magnitude of the discrepancy between the components of the vectors **Ab** and **x**.

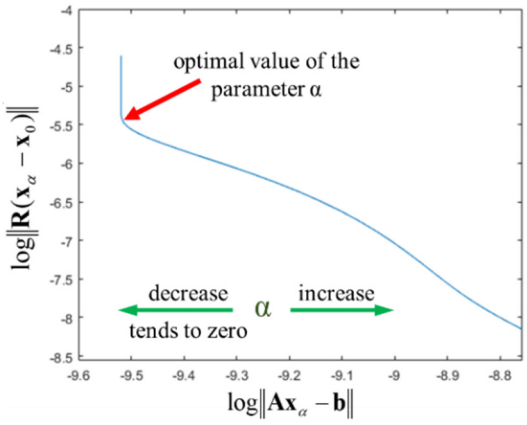

Fig. 4. Example of an *L-curve* (*own research*)

2. Experiment

2.1. Description of the tested beam and experimental setup

Ultrasonic testing was performed on a steel fiber-reinforced UHPC (Ultra-High Performance Concrete) beam with dimensions of 0.2 m × 0.24 m × 6.0 m (height × width × length). The exact dimensions of the beam under investigation are shown in Figure 5, and the experimental test setup is presented in Figure 6.

The beam was reinforced with conventional reinforcing bars and steel fibres of type DG 12.5/0.3-E304, with a length of 12.5 mm and a diameter of 0.30 mm. The steel fibre content in the beam was 2.1 %. The concrete had a compressive strength of approximately 238 MPa (Bońkowski, 2023). The longitudinal reinforcement consisted of four Ø12 bars at the bottom and four Ø12 bars at the top. The transverse reinforcement was provided by two-legged Ø8 stirrups with a centre-to-centre spacing of 150 mm.

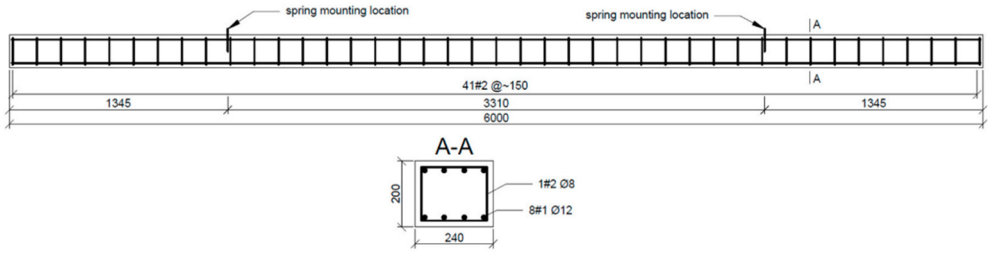

Fig. 5. Geometry of the analysed beam (dimensions in mm) (Bońkowski, 2020)

Fig. 6. View of the experimental setup (*own photo*)

The beam was subjected to static loading in 13 cycles according to the scheme shown in Figure 7, with the maximum load being successively increased in each cycle. Measurements of the longitudinal wave travel time were carried out up to the 11th cycle. In the last two load cycles, severe signal scattering prevented a reliable determination of the travel times.

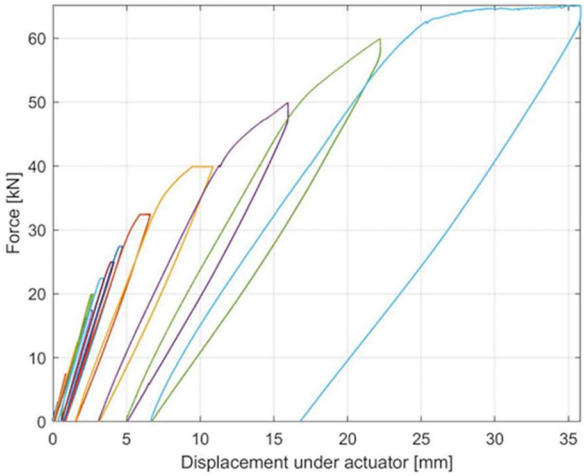

Stage	Force [kN]
0	-
1	3,13
2	7,48
3	12,46
4	17,49
5	19,97
6	22,47
7	24,98
8	27,48
9	32,51
10	39,94
11	49,94

Fig. 7. Force – displacement relationship for the UHPC beam. Table indicates maximum forces applied in the first eleven stages (*own study based on* Bońkowski, 2023)

Before the first loading (stage 0) and before each of the first 11 cycles (stages 1-11), the longitudinal wave travel time was measured for 14 transmitter-receiver point pairs (Fig. 8). The measurements were performed along a horizontal line of points spaced at 11 cm intervals, located 7 cm above the bottom edge of the beam, and were always taken after the beam had been completely unloaded.

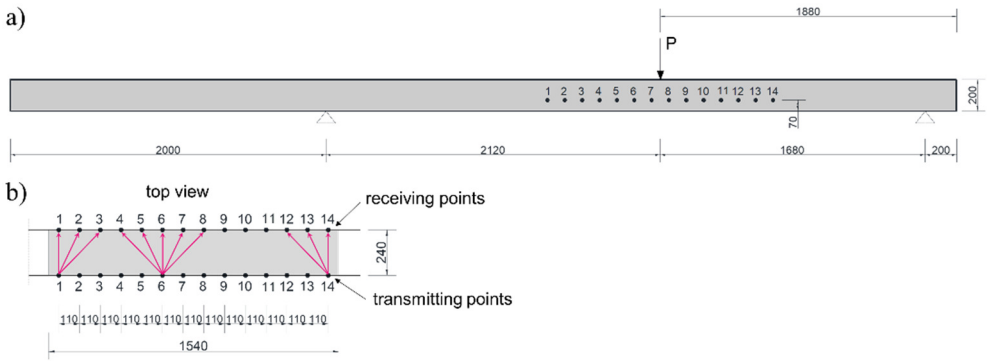

Fig. 8. a) Longitudinal view of the investigated element, b) Localisation of the measuring points in the UHPC beam (dimensions in mm) (*own study*)

Time-of-flight measurements were taken for up to two receiver points located diagonally with respect to each transmitting point. The longitudinal wave travel times between the predefined transmitter–receiver pairs were recorded using ultrasonic transducers mounted on opposite faces of the beam (Fig. 9). Transducers with a centre frequency of 150 kHz were used, and each measurement configuration was repeated three times.

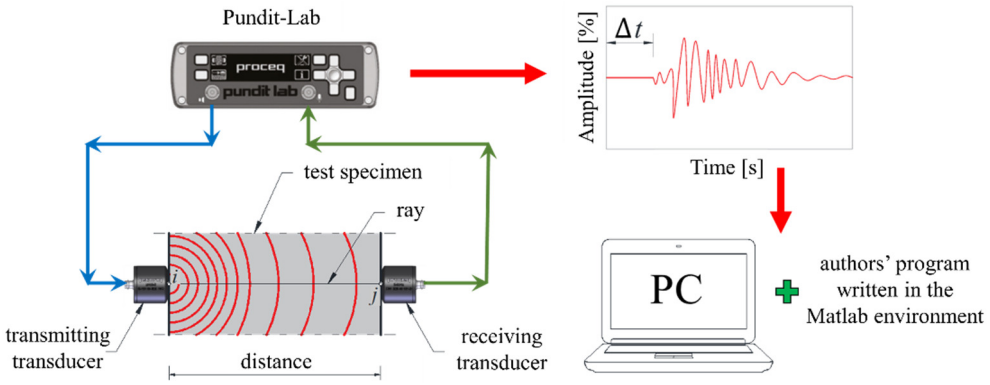

Fig. 9. Schematic of time-of-flight measurement for a single ultrasonic ray (Tatara, 2019)

Moreover, based on the measured travel times, additional "synthetic" time-of--flight values were generated by polynomial approximation at locations between the original measurement points. In particular, four equally spaced intermediate points were introduced between each pair of actual measurement positions.

2.2. Imaging of brittle damage in the UHPC beam

The reconstructed velocity distribution maps, obtained by solving system (4) with a Tikhonov-regularised *Least-Squares* algorithm in which the regularisation matrix **R** implements a discrete second-order differential operator, are shown in Figures 10 and 11. The inversion was performed on a grid of 120 rectangular cells (5 in the vertical direction and 24 in the horizontal direction).

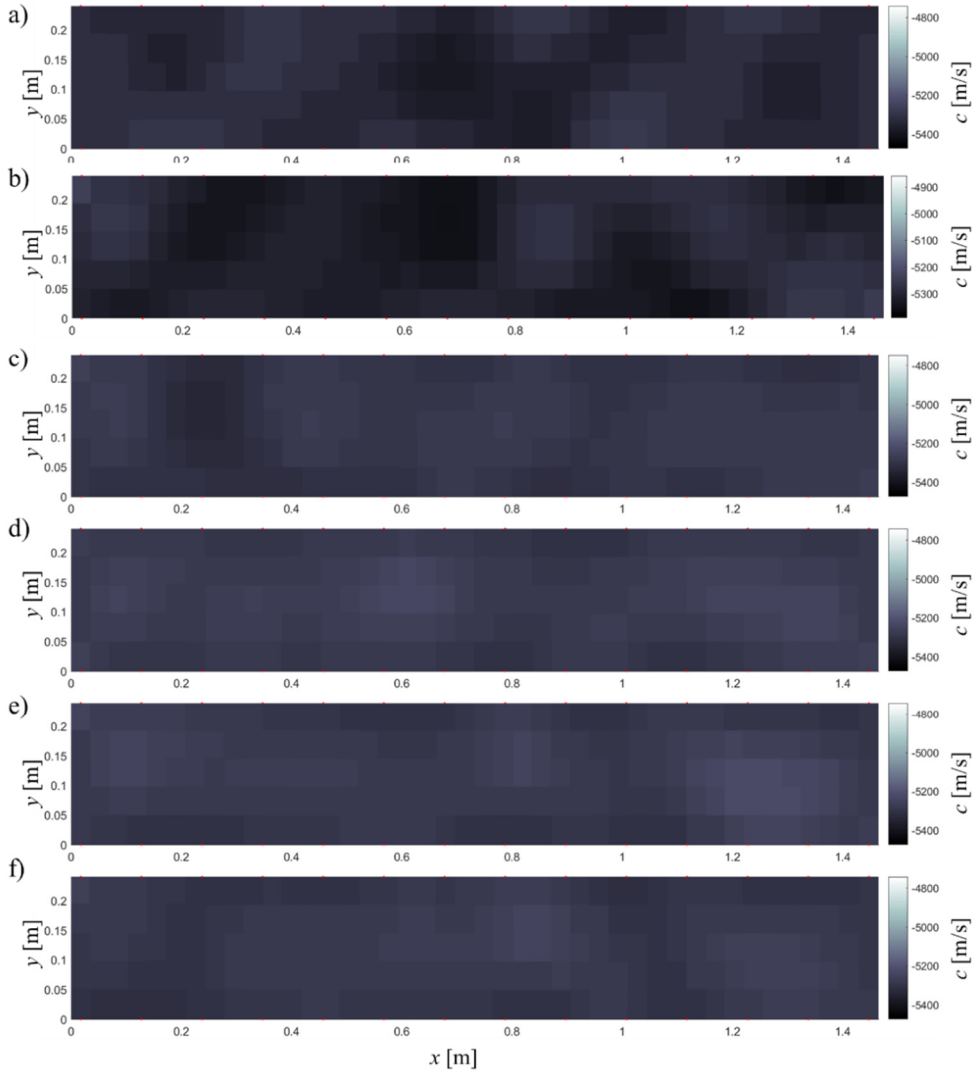

Fig. 10. Tomographic reconstructions of longitudinal ultrasonic wave velocity distributions at successive stages: a) stage 0, b) stage 1, c) stage 2, d) stage 3, e) stage 4, f) stage 5 (*own research*)

To ensure that the number of equations in system (2) was not smaller than 120 (the number of unknown cell values), the tomographic images were computed using

both the measured ultrasonic travel times and additional values obtained from polynomial interpolation between the measurement points arranged according to the layout shown in Figure 8.

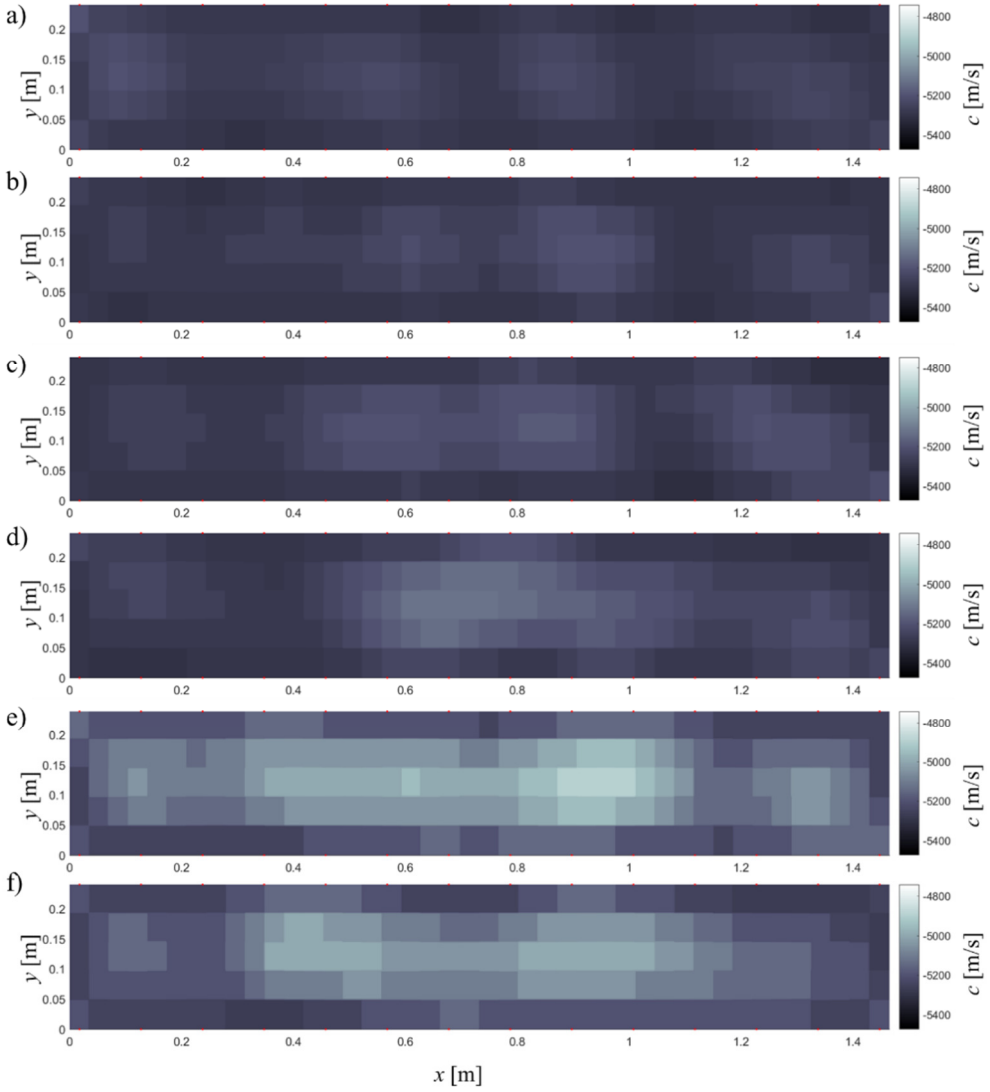

Fig. 11. Tomographic reconstructions of longitudinal ultrasonic wave velocity distributions at successive stages: a) stage 6, b) stage 7, c) stage 8, d) stage 9, e) stage 10, f) stage 11 (*own research*)

On the velocity maps shown in Figures 10 and 11, it can be seen that during the first two stages the beam exhibits slight stiffness degradation due to the onset of microcracking. From the 3rd stage onward, the reconstructed maps reveal the formation of localised damaged zones in the vicinity of the applied load, which become clearly pronounced after the 9th loading stage. Figure 12 illustrates the evolution of

cracking in the investigated region over successive loading stages (up to and including stage 11), whereas Figure 13 shows photographs of the examined zone of the UHPC beam after completion of the ultrasonic measurements. Note that apart from ultrasonic tests, the beam was also tested with a dynamic actuator. This can explain the appearance of cracks in the upper part of the beam after initial load stages. As can be observed, visible cracks in the lower part of the UHPC beam appeared only after the 4th loading stage. The locations of the degraded regions identified on the reconstructed velocity maps are largely consistent with those revealed by visual inspection (Fig. 12).

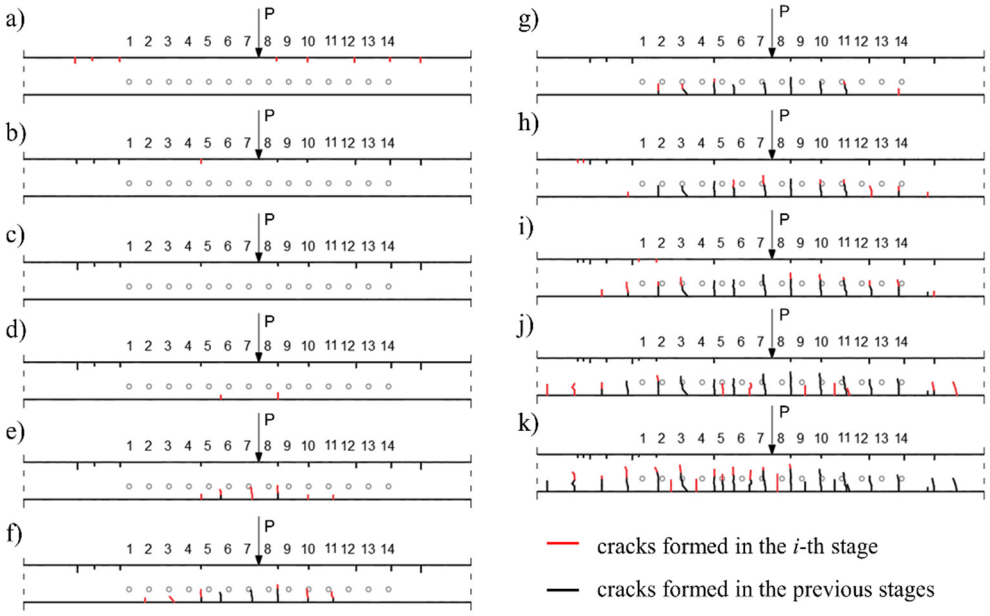

Fig. 12. Evolution of cracks in the investigated area of beam for each damage state: a) stage 1, b) stage 2, c) stage 3, d) stage 4, e) stage 5, f) stage 6, g) stage 7, h) stage 8, i) stage 9, j) stage 10, k) stage 11, source (*own study based on* Bońkowski, 2023)

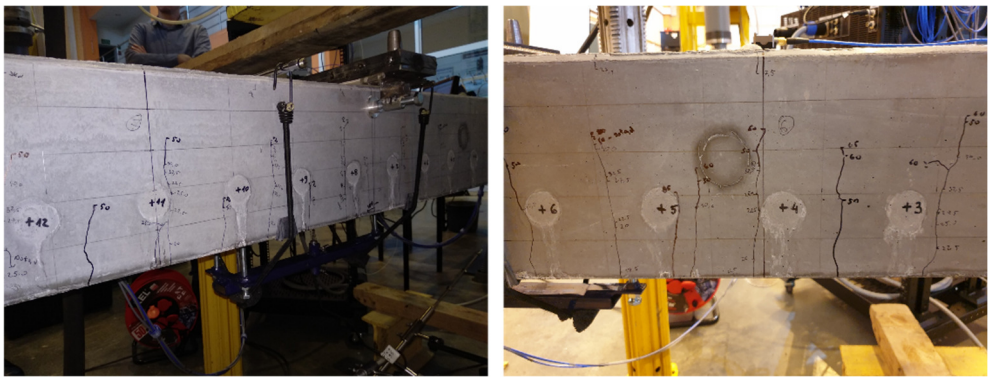

Fig. 13. View of the experimental setup (*own photo*)

Summary and conclusions

The development of non-destructive testing and diagnostic techniques in civil engineering remains one of the key directions of contemporary research. The experimental results obtained for the steel fibre-reinforced UHPC beam have shown that applying the Tikhonov-regularised least-squares method to solve the tomographic inverse problem yields qualitatively more satisfactory maps of ultrasonic wave velocity distributions. In light of the conducted investigations, ultrasonic transmission tomography, focused on measuring the spatial distribution of wave velocity in concrete, including elements made of UHPC, appears to be particularly promising for damage localisation in such members.

The results also indicate that the proposed investigation approach can be successfully applied to the diagnostic assessment of UHPC concrete elements. It should be emphasised, however, that the findings presented in this study are of a preliminary nature and require further in-depth analysis and validation through extended experimental campaigns before they can be fully generalised and widely implemented in engineering practice.

Acknowledgements

The UHPC beam subjected to ultrasonic testing was financed under the National Science Centre (NCN), Poland, grant no. 2018/02/X/ST8/02950.

Bibliography

Bońkowski, P.A., Bobra, P., Zembaty, Z. & Jędraszak, B. (2020) Application of rotation rate sensors in modal and vibration analyses of reinforced concrete beams. *Sensors*, 20, 17, 4711. DOI: 10.3390/s20174711

Bońkowski, P.A. (2023) *Application of Rotation Rate Sensors for Structural Health Monitoring of Reinforced Concrete Beams*. Opole, Oficyna Wydawnicza Politechniki Opolskiej.

Drobiec, Ł., Jasiński, R. & Piekarczyk, A. (2010) *Diagnostyka konstrukcji żelbetowych*. T.1, Warszawa, PWN.

Gordon R., Bender R. & Herman G.T. (1970) Algebraic reconstruction techniques (ART) for three-dimensional electron microscopy and X-ray photography. *Journal of Theoretical Biology*, 29(3), 471-481.

Hansen, P.C. & Saxild-Hansen, M. (2012) AIR tools – a MATLAB package of algebraic iterative reconstruction methods. *Journal of Computational and Applied Mathematics*, 236(8), 2167-2178.

Hounsfield, G.N. (1973) Computerized transverse axial scanning (tomography): Part 1. Description of system. *The British Journal of Radiology*, 46(552), 1016-1022.

Kak, A. & Slaney, M. (1999) *Principles of Computerized Tomographic Imaging*. New York, IEEE.

Karatosun, S., Thygesen, K.I.M., Gustafsson, K., Christiansen, A.G. & Ottosen, L.M. (2025) Development and validation of an NDT-based reuse assessment guideline for structural concrete elements. *E-Journal of Nondestructive Testing*, 30(10). DOI: 10.58286/31670.

Lampe, J. & Voss, H. (2010) Solving regularized total least squares problems based on eigenproblems. *Taiwanese Journal of Mathematics*, 14(3A), 885-909.

Lawson, C.L. & Hanson, R.J. (1995) *Solving Least Squares Problems*. Philadelphia, SIAM.

Lewińska-Romicka, A. (2001) *Badania nieniszczące. Podstawy defektoskopii*. Warszawa, WNT.

Miller, K. (1970) Least squares methods for ill-posed problems with a prescribed bound. *SIAM Journal of Mathematical Analysis*, 1, 52-74.

Opieliński, K. & Gudra, T. (2002) Uniwersalne stanowisko badawcze do ultradźwiękowej tomografii transmisyjnej. *Badania Materiałów* (3).

Perkowski, Z., Tatara, K. & Czabak, M. (2018) Imaging elastic degradation in reinforced concrete slab using methodology of ultrasonic tomography and Tikhonov regularization. In: Shell Structure: Theory and Applications, 4. CRC Press/Balkema, 445-448.

Phillips, D.L. (1962) A technique for the numerical solution of certain integral equations of the first kind. *Journal of the Association for Computing Machinery*, 9, 84-97.

Polak, A.G. & Mroczka, J. (2007) Regularyzacja identyfikacji obiektów złożonych opisanych modelami nieliniowymi. *Pomiary Automatyka Kontrola*, 53, 9 bis, 190-193.

Polakowski, K. & Sikora, J. (2016) *Podstawy matematyczne obrazowania ultradźwiękowego*. Lublin, Politechnika Lubelska.

Skubalska-Rafajłowicz, E. (2011) *Sieci neuronowe w przetwarzaniu strumieni danych. Struktury sieci i algorytmy uczenia*. Wrocław, Oficyna Wydawnicza Politechniki Wrocławskiej.

Smedt, M.D., Wilder, K.D., Verstrynge, E. & Vandewalle, L. (2018) Experimental analysis of monotonic and cyclic pull-out of steel fibres by means of acoustic emission and X-ray microfocus computed tomography. *Proceedings*, 2(8), 396. DOI: 10.3390/ICEM18-05226.

Śliwiński, A. (2001) *Ultradźwięki i ich zastosowania*. Warszawa, WNT.

Tatara, K. (2019) *Identyfikacja kruchych uszkodzeń w konstrukcjach betonowych z wykorzystaniem tranmisyjnej tomografii ultradźwiękowej i algorytmu Dijkstry*. A doctoral dissertation prepared under the supervision of Zbigniew Perkowski, PhD, Eng. Opole University of Technology, Faculty of Civil Engineering and Architecture.

Uhl, T. (2010) *Współczesne metody monitorowania i diagnozowania konstrukcji*. In: *Polskie i światowe osiągnięcia nauki: nauki techniczne*, 6. Fundacja im. Wojciecha Świętosławskiego na rzecz Wspierania Nauki i Rozwoju Potencjału Naukowego w Polsce, 193-254.

Voss, H. (2010) *Regularization of Least Squares Problems*. https://www.mat.tuhh.de/lehre/material/Regularisierung.pdf.